



HAL
open science

Speed robust design of switched reluctance motor for electric vehicle system

Moussa Boukhnifer, Ahmed Chaibet, Nadir Ouddah, Eric Monmasson

► **To cite this version:**

Moussa Boukhnifer, Ahmed Chaibet, Nadir Ouddah, Eric Monmasson. Speed robust design of switched reluctance motor for electric vehicle system. *Advances in Mechanical Engineering*, 2017, 9 (11), pp.168781401773344. 10.1177/1687814017733440 . hal-01733299

HAL Id: hal-01733299

<https://hal.science/hal-01733299>

Submitted on 20 Dec 2018

HAL is a multi-disciplinary open access archive for the deposit and dissemination of scientific research documents, whether they are published or not. The documents may come from teaching and research institutions in France or abroad, or from public or private research centers.

L'archive ouverte pluridisciplinaire **HAL**, est destinée au dépôt et à la diffusion de documents scientifiques de niveau recherche, publiés ou non, émanant des établissements d'enseignement et de recherche français ou étrangers, des laboratoires publics ou privés.



Distributed under a Creative Commons Attribution - NonCommercial 4.0 International License

Speed robust design of switched reluctance motor for electric vehicle system

Advances in Mechanical Engineering
2017, Vol. 9(11) 1–14
© The Author(s) 2017
DOI: 10.1177/1687814017733440
journals.sagepub.com/home/ade


Moussa Boukhni¹, Ahmed Chaibet¹, Nadir Ouddah¹
and Eric Monmasson²

Abstract

The strong nonlinear and uncertain parameters of the switched reluctance motor make the traditional controllers difficult to ensure a good performances and stable operation under diverse operating conditions. This work focuses on developing of a new robust design control for switched reluctance motor drives for electrical vehicle to attenuate the effect of disturbances and parameter uncertainties. For this, we have adopted the cascade control architecture (velocity–torque) using two different H_∞ syntheses (standard and fixed H_∞ approaches). The first controller of velocity in the outer control loop products the total torque of switched reluctance motor. Hence, a linear equivalent mechanical dynamic is obtained. In the inner control loop, the phase reference current is determined using the torque–angle–current ($T - \theta - i$) characteristics stored in lookup table, and the torque is regulated indirectly through the second controller of current. For each control loop, two H_∞ synthesis approaches are used and compared by μ analysis. The simulation and experimental results demonstrate the effectiveness of the designed robust controllers and confirm the ability of the proposed strategies.

Keywords

Electrical vehicle, switched reluctant motor drives, fixed H_∞ robust control, μ analysis

Date received: 15 December 2016; accepted: 31 August 2017

Handling Editor: Xiaoyuan Zhu

Introduction

The electrification of vehicles presents an interesting solution to achieve ambitious objectives allowing to reduce fuel consumption, limit environment impacts, and diversify energy sources. Therefore, several research activities are focusing on hybrid electric vehicles (HEV) and electric vehicles (EVs). The aim is to develop new architectures to improve current technology's performances with respect to cost, efficiency, size, mass, reliability, security, and safety constraints.^{1,2} The development and progress of EV is directly related to its electric powertrain. A typical electric powertrain includes an energy source, a power inverter, and an electrical machine. The energy source is basically a high-voltage battery, but it can be a hybrid source (e.g.

fuel cell and battery). The aim of the EV is to operate over a wide torque speed range in response to various driving conditions. The challenge for the EV traction machine design is to produce high torque at the startup, at standstill, or low speed in order to provide required acceleration and climbing capability.³ Brushless DC

¹Ecole Supérieure des Techniques Aéronautiques et de Construction Automobile, Saint-Quentin-en-Yvelines, France

²Université de Cergy-Pontoise, Cergy, France

Corresponding author:

Moussa Boukhni¹, Ecole Supérieure des Techniques Aéronautiques et de Construction Automobile, ESTACA Campus Paris-Saclay, 12, avenue Paul Delouvrier, 78066 Saint-Quentin-en-Yvelines, France.
Email: moussa.boukhni¹@estaca.fr



motor, induction motor, permanent magnet synchronous machine (PMSM), and switched reluctance motor (SRM) are all used in EV. An evaluation of trade-offs between the efficiency, weight and cost, cooling, maximum speed, fault tolerance, safety, and reliability for the motors mentioned above has been accomplished in Xue et al.,⁴ and SRM drives were considered as the most appropriate candidate for EVs by evaluating an optimal balance of these criteria. However, SRM has larger torque ripple compared to other types of motors. These drawbacks can be coped with optimal design and a good control of the motor. Furthermore, the behavior of the SRM and its drive is highly nonlinear, and hence modern control techniques are needed to control the SRM system to achieve high dynamical performance. During the last two decades, various control techniques have been developed for the control of SRM such as feedback-linearization control, variable structure and sliding mode control, adaptive control, and neural and fuzzy logic control.⁵⁻⁸ These control methods require an accurate model of the motor or/and a high online computational requirements. As developing an accurate nonlinear model for SRM is difficult and subject to error due to manufacturing tolerances, and parameter drift during operation, the developed controller should be robust against model inaccuracies and parameter variations. This work aims to propose a robust controller design of SRM; this controller is intended for speed tracking in EV applications. A cascade control structure is adopted, with an inner torque loop and an outer velocity loop. The outer control loop provides the total reference torque, which is regulated indirectly in the inner control loop through the current regulation. Instead of using conventional time-averaged torque control, the control method on an instantaneous basis is applied to reduce the torque ripple at low speeds which is an important issue to avoid mechanical fatigue of the system and satisfy the comfort in the EV. Modern robust H_∞ control theory⁹⁻¹³ has been used for its well-known robustness against parameter variations and model uncertainties. Standard and fixed-order H_∞ synthesis approaches are used and compared for both speed and current control loops. The outline of this article is as follows: section "SRM model and controller design" presents the full nonlinear model of the SRM and describes the proposed control architecture. Section "Robust control methodology" discusses the design of both speed and current controllers, and the two cases are shown for each control loop: the first one is a full-order H_∞ controller, and the second one is a fixed structure H_∞ controller. Section "Robust control and robustness analysis" is devoted to the robust control design of SRM drive, and the robust stability of the proposed controllers with respect to parameter uncertainties is studied. Performance of these controllers is then verified by simulation, and experimental

Table 1. Switched reluctance motor parameters.

Parameters	Values
Nominal power	1.2 kW
Nominal speed	3000 r/min
Nominal voltage	24 V
Number of rotor poles	6
Number of stator poles	8
Stator resistance	0.049 Ω
Moment of inertia	6.8 kg m ²
Stator teeth arc	19.8 \hat{A}°
Rotor teeth arc	20.65 \hat{A}°
Air gap length	0.8 mm

results are shown in section "Simulation and experimental results." Finally, conclusion of this work is addressed in section "Conclusion."

SRM model and controller design

Mathematical model of the system

The parameters of SRM are given in Table 1.

The main principle for SRMs modeling is based on the magnetic position curve, which shows the linking flux versus phase current for different rotor angles (see Figure 1). The full mathematical model of the SRM is described below. The phase voltages are expressed as follows

$$V_j = Ri_j + \frac{d\phi_j(\theta, i_j)}{dt} \quad (1)$$

in which V_j stands for j th-phase winding voltage, i_j for the j th-phase current, ϕ_j for the linking flux, and R for the ohmic resistance of the phase winding. The coupling between adjacent windings is neglected, and the flux linkage can be written as

$$\begin{aligned} \phi_j(\theta, i_j) &= L(\theta, i_j)i_j \\ \frac{d\phi_j(\theta, i_j)}{dt} &= L(\theta, i_j) \frac{\partial i_j}{\partial t} + i_j \frac{\partial L(\theta, i_j)}{\partial t} \\ \frac{d\phi_j(\theta, i_j)}{dt} &= L(\theta, i_j) \frac{\partial i_j}{\partial t} + i_j \left(\frac{\partial L(\theta, i_j)}{\partial \theta} \frac{\partial \theta}{\partial t} + \frac{\partial L(\theta, i_j)}{\partial i_j} \frac{\partial i_j}{\partial t} \right) \end{aligned} \quad (2)$$

$$V_j = Ri_j + \left(L_j(\theta, i_j) + i_j \frac{\partial L(\theta, i_j)}{\partial i_j} \right) \frac{\partial i_j}{\partial t} + i_j \omega \frac{\partial L_j(\theta, i_j)}{\partial \theta} \quad (3)$$

Equation (1) can be written in the following form

$$V_j = Ri_j + L_{inc}(\theta, i_j) \frac{\partial i_j}{\partial t} + E \quad (4)$$

with

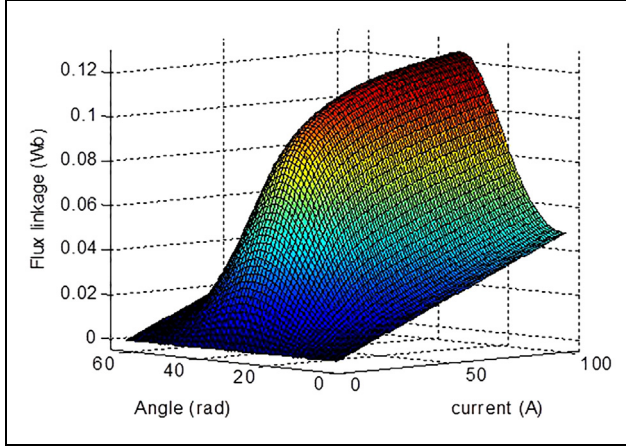


Figure 1. Flux linkage curve.

$$L_{inc} = L_j(\theta, i_j) + i_j \frac{\partial L(\theta, i_j)}{\partial i_j} \text{ and } E_j = i_j \omega \frac{\partial L_j(\theta, i_j)}{\partial \theta}$$

L_{inc} is the increasing inductance and E is the back electromotive force (emf) coefficient. L_{inc} and E are dependent on current and rotor angular position. The produced torque on the shaft is equal to the sum of individual torque produced by all phases

$$T = \sum_{j=1}^4 T_j(\theta, i_j) \quad (5)$$

where T_j is the torque of the j th phase.

$$T_j(\theta, i_j) = \frac{\partial W_c(\theta, i_j)}{\partial \theta} \quad (6)$$

with W_c is co-energy

$$W_c(\theta, i_j) = \int_0^{i_j} \phi(\theta, i_j) di_j \quad (7)$$

Furthermore, the mechanical equations will be as follows

$$\omega = \frac{d\theta}{dt} \quad (8)$$

$$\frac{d\omega}{dt} = \frac{1}{J} (T(\theta, i_j) - T_L - f\omega) \quad (9)$$

where ω is the angular speed, T_L is the load torque, f is the friction coefficient, and J is the moment of inertia. However, finding a lumped function for $T(\theta, i_j)$ is very difficult and demands numerical or experimental data for a specific motor.¹⁴ The aforementioned data have been deduced from the flux linkage curve using equation (5) (see Figure 2).

Finally, the dynamic model of SRM is given by

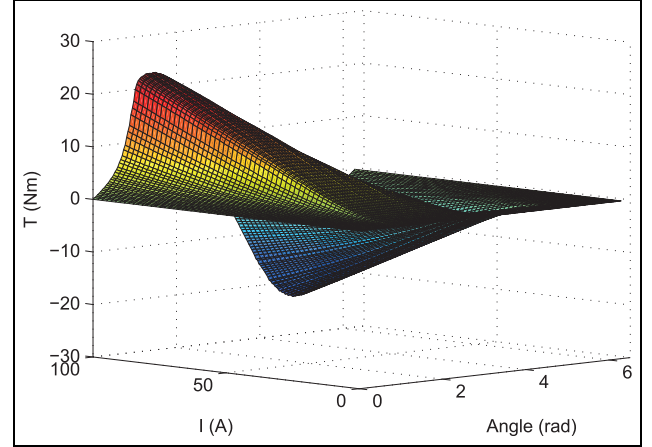


Figure 2. Static torque characteristic for one phase.

$$\begin{cases} \omega = \frac{d\theta}{dt} \\ \frac{d\omega}{dt} = \frac{1}{J} (T(\theta, i_j) - T_L - f\omega) \\ \frac{\partial i_j}{\partial t} = \frac{1}{L_{inc}(\theta, i_j)} (V_j - R_{i_j} - E_j) \end{cases} \quad (10)$$

Controller structure

The adopted cascade structure to design a speed tracking controller for SRM drive is given in Figure 3. The total produced torque of SRM has been considered as the output of the velocity controller. Hence, a linear equivalent mechanical dynamic is obtained.¹⁵

The expected phase torque is obtained through a torque sharing function (TSF; Figure 4). Instead of using conventional time-averaged torque control, the control method on an instantaneous basis is applied. This approach uses the torque–angle–current (T – θ – i) characteristics obtained by finite element method (FEM) and stored in a tabular form, so the reference phase current can be determined by both the torque requirement and position measurement.¹⁶ Finally, under the current control, the actual phase current follows the expected one well. In addition to the advantages deriving from the separation of low-dynamic (velocity) and high-dynamic signals (currents), the cascade structure uses an intermediate TSF.

The TSF distributes the demanded torque among two neighboring phases, and ensure a smooth growth and the drop of the torque demand for each phase. Thereby, preventing the shaft torque oscillations during commutation and avoiding excessive radial and tangential forces causing audible noise. The TSF with a cosine function has been used in this work, similar to the one proposed earlier in Tingna et al.¹⁷ The function TSF is given by

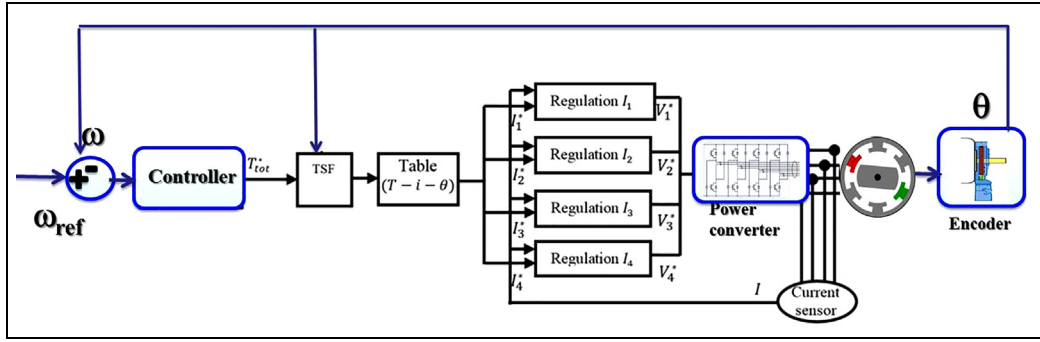


Figure 3. The block diagram of the SRM drive.

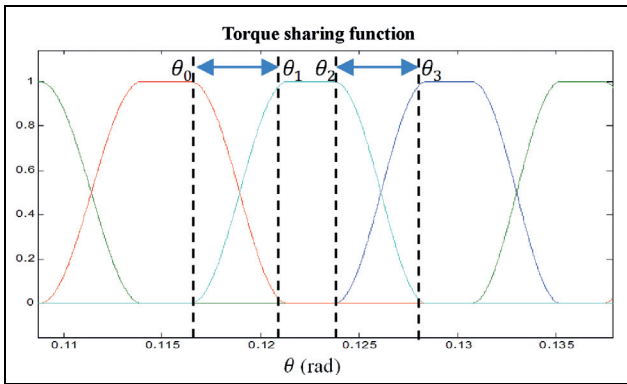


Figure 4. Torque sharing function.

$$F_j(\theta) = \begin{cases} 0.5 - 0.5 \cos nN_r(\theta - \theta_0), & \theta_{0j} \leq \theta \leq \theta_{1j} \\ 1, & \theta_{1j} \leq \theta \leq \theta_{2j} \\ 0.5 + 0.5 \cos nN_r(\theta - \theta_0), & \theta_{2j} \leq \theta \leq \theta_{3j} \\ 0, & \text{Others} \end{cases} \quad (11)$$

where $F_j(\theta)$ is the j th-phase torque distribution function ($j = 1, 2, 3, 4$), n is the number of motor phase, N_r is the number of rotor pole, θ_{0j} is the j th-phase opening angle, θ_{1j} is the j th-phase rotor position when the torque stops rising, θ_{2j} is the j th-phase breaking angle, and θ_{3j} is the j th-phase rotor position when the torque reduces to zero. The j th-phase expectation of torque is expressed as

$$T_{j\text{ref}} = T_j F_j(\theta) \quad (12)$$

Robust control methodology

H_∞ problem

For given $G(s)$ and $\gamma > 0$, the H_∞ problem is to find $K(s)$ which

- Stabilizes the loop system of Figure 5 internally;

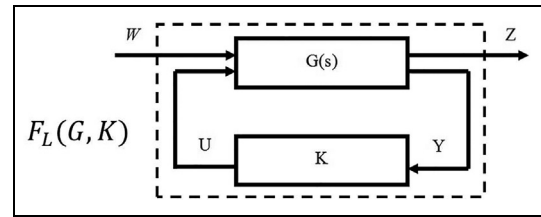


Figure 5. H_∞ problem.

- Maintains the norm $\|F_L(G, K)\|_\infty < \gamma$ with $F_L(G, K)$ defined as the transfer function of exits Z according to inputs W .

where G is the generalized plant and K is the controller. Only finite-dimensional linear time invariant (LTI) systems and controllers will be considered in this article. The generalized plant G contains what is usually called the plant in a control problem plus all weighing functions. The signal W contains all external inputs, including disturbances, sensor noise, and commands; the output Z is an error signal; Y is the measured variables; and U is the control input. The diagram is also referred to as a linear fractional transformation (LFT) on K , and G is called the coefficient matrix for the LFT. The resulting closed-loop transfer function from W to Z is denoted by T_{zw} .

The problem of H_∞ standard is to synthesize a controller K which stabilizes the system G and minimizes the norm H_∞ of T_{zw}

$$G = \begin{bmatrix} A & B_1 & B_2 \\ C_1 & 0 & D_{12} \\ C_2 & D_{21} & 0 \end{bmatrix} \quad (13)$$

The following assumptions are made:

1. (A, B_1) is stabilizable, and (C_1, A) is detectable;
2. (A, B_2) is stabilizable, and (C_2, A) is detectable;
3. $D_{12}^T [C_1 \ D_{12}] = [0 \ I]$;
4. $[B_1 \ D_{21}]^T D_{21}^T = [0 \ I]^T$.

The problem of H_∞ standard is to synthesize a controller K which stabilizes the system G and minimizes the H_∞ norm of $\|T_{zw}\|_\infty$. Recall that the H_∞ controller is given by

$$K_\infty = \begin{bmatrix} \hat{A}_\infty & -Z_\infty L_\infty \\ F_\infty & 0 \end{bmatrix} \quad (14)$$

$$\hat{A} = A + \gamma^{-2} B_1 B_1^T X_\infty + B_2 F_\infty C_2$$

$$F_\infty = -B_2^T X_\infty, \quad L = -Y_\infty C_2, \quad Z_\infty = (I - \gamma^{-2} Y_\infty X_\infty)^{-1}$$

where $X_\infty = Ric(H_\infty)$ and $Y_\infty = Ric(J_\infty)$

The necessary and sufficient conditions for the existence of an admissible controller such that of $\|T_{zw}\|_\infty < \gamma$ are as follows

1. $H_\infty \in \text{dom}(Ric)$ and $X_\infty = Ric(H_\infty) \geq 0$;
2. $J_\infty \in \text{dom}(Ric)$ and $Y_\infty = Ric(J_\infty) \geq 0$;
3. $\rho(X_\infty Y_\infty) < \gamma^2$.

The Hamiltonian matrices are defined as

$$H_\infty = \begin{bmatrix} A & \gamma^{-2} B_1 B_1^T - B_2 B_2^T \\ -C_1^T C_1 & -A^T \end{bmatrix}$$

$$J_\infty = \begin{bmatrix} A^T & \gamma^{-2} C_1 C_1^T - C_2^T C_2 \\ -B_1 B_1^T & -A \end{bmatrix}$$

Standard mixed sensitivity design procedure

Mixed sensitivity optimization is a powerful design tool for linear single-degree-of-freedom feedback systems. It allows simultaneous design for performance and robustness and relies on shaping the critical closed-loop sensitivity functions with frequency-dependent weights.⁹ Figure 6 presents the generalized plant for H_∞ mixed sensitivity problem, where $G(s)$ is the open-loop plant; $K(s)$ is the controller to be designed; and $W_1(s)$, $W_2(s)$, $W_3(s)$ are weights for specifying the system performance. d is the disturbance input, u is the control input, y is the measured output, e_1 and e_2 are regulated outputs, and r is the reference input.

The transfer matrix from r and d to e_1 and e_2 is given by

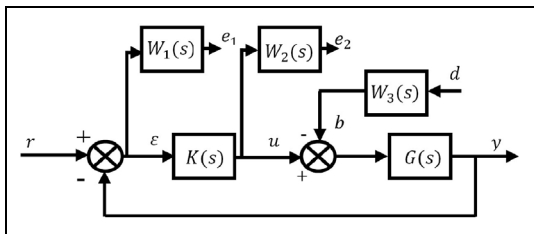


Figure 6. Mixed sensitivity configuration.

$$\begin{bmatrix} E_1(s) \\ E_2(s) \end{bmatrix} = \begin{bmatrix} W_1 S(s) & W_1(s) S(s) G(s) W_3(s) \\ W_2 K(s) S(s) & W_2(s) T(s) W_3(s) \end{bmatrix} \begin{bmatrix} R(s) \\ D(s) \end{bmatrix} \quad (15)$$

where

$$S = (1 + GK)^{-1}$$

is the sensitivity function and $T = KGS$ is the complementary sensitivity function.

The resulting H_∞ standard problem is: for γ as small as possible, find a stabilizing controller $K(s)$ such as

$$\left\| \begin{bmatrix} W_1(s) S(s) & W_1(s) S(s) G(s) W_3(s) \\ W_2(s) K(s) S(s) & W_2(s) T(s) W_3(s) \end{bmatrix} \right\|_\infty < \gamma \quad (16)$$

Performance and robustness are characterized by various well-known closed-loop functions, in particular the sensitivity function S , the complementary sensitivity function T , and the input sensitivity function KS .

The motivation for the mixed sensitivity approach is that a controller must satisfy condition (16) and also satisfies that each input of the matrices $W_1(s)$, $W_2(s)K(s)S(s)$, $W_1(s)S(s)G(s)W_3(s)$, and $W_2(s)T(s)W_3(s)$ is bounded by γ as well, which is usually the original goal.

The weighting functions $W_1(s)$, $W_2(s)$, and $W_3(s)$ are selected in accordance with the basic requirement of mixed sensitivity design.¹³ Since $W_1(s)$ is related to the performance objective of the error sensitivity function $S(s)$, it should be a low-pass filter to reduce the error sensitivity in the low frequency range for output disturbance rejection. $W_2(s)$, on the other hand, should be a high-pass filter in order to guarantee the stability of the controlled system under diverse operating conditions. An additional disturbance weighting function, $W_3(s)$, is used to represent bounds on the disturbance, and it can be set to a constant or chosen as a high-pass filter.

Fixed structure controller design procedure

The fixed structure controller is interesting because lower-order controller could be important for real implementation where the control system structure and complexity are constrained. In this article, the proposed method uses sub-gradient calculus to solve the H_∞ optimization problem by first minimizing the spectral abscissa of the closed-loop system to find parameters for a stable controller.¹⁸ These parameters are used as a starting point when optimizing locally to minimize the H_∞ norm. The synthesis procedure is reminiscent of standard H_∞ synthesis but differs in one key aspect, namely, the special structure of the controller. Using this function, the controller structure and its order are fixed before the synthesis. The function inputs allow

for simple gain controllers, fixed state space, or transfer functions.

However, there exist new MATLAB tools for structured H_∞ synthesis (*Hinfstruct* and *Hifoo*) in Robust Control Toolbox, which allows the controller order to be fixed. The design problem is to minimize the H_∞ norm of the transfer function for the closed-loop plant. This is a difficult optimization problem due to the non-convexity and nonsmoothness of the objective function. The purpose is to optimize the criterion given by equation (17)

$$f(\theta) := \|F_L(P, K(\theta))\|_\infty = \max_{\omega \in \mathbb{R}^n} \bar{\sigma} \left(C_{cl}(K(\theta))(j\omega I - A_{cl}(K(\theta)))^{-1} B_{cl}(K(\theta)) + D_{cl}(K(\theta)) \right) \quad (17)$$

where $\bar{\sigma}$ is the largest singular value and $K(\theta)$ is the controller which is structured with the parameter $\theta \in \mathbb{R}^n$

$$T_{w \rightarrow z} : \begin{bmatrix} \dot{\tilde{x}} \\ z \end{bmatrix} \begin{bmatrix} A_{cl}(K(\theta)) & B_{cl}(K(\theta)) \\ C_{cl}(K(\theta)) & D_{cl}(K(\theta)) \end{bmatrix} \begin{bmatrix} \tilde{x} \\ w \end{bmatrix} \quad (18)$$

where A_{cl} , B_{cl} , C_{cl} , and D_{cl} are the closed matrices of the plant G .

Robust control and robustness analysis

Robust control design of SRM drive

The proposed control architecture is composed of two cascaded loops: the outer loop is used for the speed tracking and provides the total reference torque. The task of the inner loop is to track the reference torque through the currents regulation. In the following sections, the design of these controllers is addressed, and two cases are shown for both speed and current loops: the first one is a full-order H_∞ controller, and the second one is a fixed structure H_∞ controller.

Speed loop controller

H_∞ standard mixed sensitivity speed controller. For mixed sensitivity solution of H_∞ control theory, the weighting functions $W_1(s)$, $W_2(s)$, and $W_3(s)$ are used to guide the H_∞ algorithm to generate a controller that meets the required specifications (good performance in tracking, antisturbance, and robustness). For our SRM speed control problem, the weighting functions are chosen as

$$\begin{aligned} W_1(s) &= \frac{s + 143}{1.43s + .143} \\ W_2(s) &= 0.15 \times \frac{8.33 \times 10^{-3}s + 10^4}{s + 10^3} \\ W_3(s) &= 0.1 \end{aligned}$$

Using the design of Figure 5, the H_∞ controller $K(s)$ is given by

$$K(s) = \frac{128.8s^2 + 1.45 \times 10^8 s + 2 \times 10^9}{s^3 + 1.57 \times 10^5 s^2 + 1.97 \times 10^8 s + 1.97 \times 10^7}$$

H_∞ fixed structure speed controller. The weighting functions chosen for the fixed structure controller synthesis are the same as in the standard mixed sensitivity synthesis, and the controller structure is then selected as second-order transfer function form. The fixed H_∞ controller is

$$K(s) = \frac{1.43 \times 10^3 s + 10^4}{s^2 + 1.28 \times 10^3 s + 128}$$

Current loop controller

H_∞ standard mixed sensitivity current controller. The same synthesis procedure is applied for the current loop, the weighting functions are given by

$$\begin{aligned} W_1(s) &= \frac{0.7s + 10^3}{s + 1} \\ W_2(s) &= 0.5 \times \frac{s + 10^4}{1.6 \times 10^{-3}s + 2 \times 10^4} \\ W_3(s) &= 0.2 \end{aligned}$$

The full-order H_∞ controller is

$$K(s) = \frac{962s^2 + 1.15 \times 10^{10} s + 1.22 \times 10^{12}}{s^3 + 4.52 \times 10^5 s^2 + 5.67 \times 10^9 s + 5.6 \times 10^4}$$

H_∞ fixed structure current controller. We proceed in the same manner as above (the standard mixed sensitivity synthesis case) to choose the weighting functions. The fixed H_∞ controller is

$$K(s) = \frac{3.86 \times 10^4 s + 2.37 \times 10^6}{s^2 + 1.3 \times 10^4 s + 1.3 \times 10^4}$$

Robustness analysis

The SRM dynamic model given by equation (10) is affected by parameter uncertainties because the stator phase inductance L and resistance R vary during system operation, and the moment of inertia J and the coefficient of friction f are not well known. In this part, we study the robust stability of cascaded control loop architecture: in the first case, we consider one mechanical uncertain dynamic with the speed feedback controller and in the second case the uncertain and variation of electric parameters, respectively, (R, L) in the current loop. The uncertain model can be represented by a general form called LFT. The uncertainty is introduced in the closed-loop nominal system by creating an augmented system with

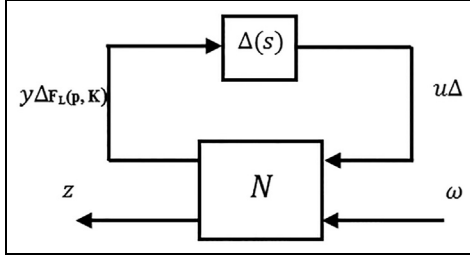


Figure 7. Nominal closed-loop model connected to uncertainty.

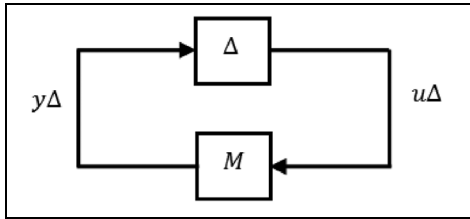


Figure 8. ΔM structure for robust stability analysis.

additional inputs and outputs used in order to connect via an upper LFT an uncertainty block Δ (see Figure 7).¹⁹ These uncertainties are grouped into a diagonal matrix and are given by the following equation

$$\Delta = \text{diag}\{\delta_1 l r_1, \dots, \delta_r l r_r\} \quad (19)$$

where

$$\delta_i \in]-1; +1[\in \mathbb{R}$$

To analyze robust stability, we can rearrange the system into the $M\Delta$ structure as you can see in Figure 8, where $M = N_{11}$ is the transfer function from the output to the input of the disturbances.

$$F = F_u(N, \Delta) : = N_{22} + N_{21}\Delta(I - N_{11}\Delta)^{-1}N_{12} \quad (20)$$

We consider parametric uncertainties on both control loops (speed and current loops), uncertainty parameters (J, f) in the speed loop and (R, L) in the current loop. An estimated $\pm 25\%$ variation on the values (J, f, R) and $\pm 40\%$ variation on the value of L are considered. In addition, a complex uncertainty ε is incorporated in both control loops in order to study robustness of the stability margins. The robustness must be now studied in relation to the set

$$\Delta'(s) = \text{diag}\{\Delta, \varepsilon\} \quad (21)$$

where $|\varepsilon| < 1$ and $\varepsilon \in \mathbb{C}$

The robustness analysis in this study is based on the computation of the structured singular value (SSV of

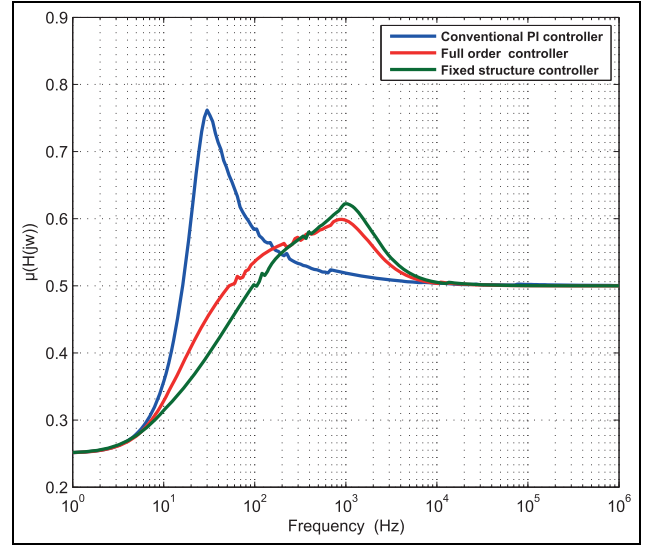


Figure 9. Maximum SSV plots for speed loop.

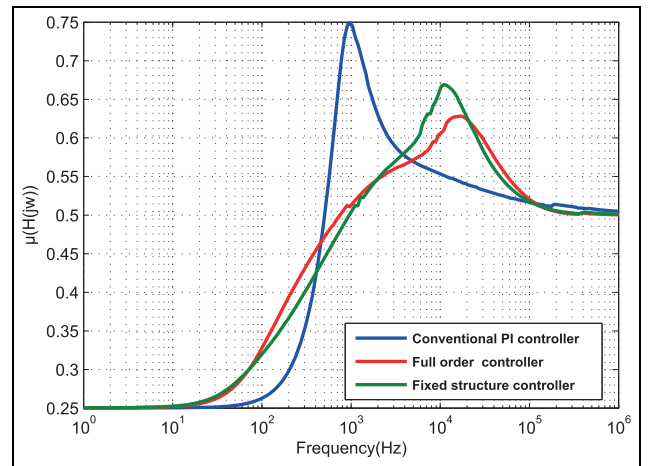


Figure 10. Maximum SSV plots for current loop.

Table 2. The robustness analysis results of the modulus margin for speed loop.

Controller	Maximum SSV values	Minimum modulus margin	Maximum uncertainty levels
H_∞ full order	0.601	0.83	166%
H_∞ fixed structure	0.622	0.8	160%
PI controller	0.761	0.65	131%

SSV: structured singular value; PI: proportional–integral.

M), that is, the μ analysis. The purpose is to ensure a margin module ≥ 0.5 to the uncertain system. The SSV is computed for the different designed controllers. Figure 9 shows the maximum SSV's plots for the speed

Table 3. The robustness analysis results of the modulus margin for current loop.

Controller	Maximum SSV values	Minimum modulus margin	Maximum uncertainty levels
H_∞ full order	0.628	0.79	159%
H_∞ fixed structure	0.669	0.74	149%
PI controller	0.769	0.65	130%

SSV: structured singular value; PI: proportional–integral.

loop, while the maximum SSV's plots for the current loop are shown in Figure 10. From these curves, we can notice that all the designed controllers of both speed and current loops guarantee good robustness margin. However, full-order H_∞ controllers achieve better robustness performance for both control loops. The overall robustness analysis results are reported in Tables 2 and 3.

Simulation and experimental results

Simulations results

The considered control architecture is evaluated with the normalized European cycle as speed reference. Normalized European cycle ECE-15 is a driving cycle designed to assess the emission levels of car engines and fuel economy in passenger cars (excluding light trucks and commercial vehicles). The proposed controllers of both speed and current loops are tested by simulations using MATLAB/Simulink. For each control loop, simulation results are compared in order to evaluate the trade-offs between performances and the structural complexity of the synthesized controllers.

Speed control. The control aim is to minimize the error between desired speed and the SRM speed. The two synthesized H_∞ controllers are tested using the normalized European cycle ECE-15. Figure 11 shows a good response of the motor speed, the system still able to follow the reference signal with a high performance (the tracking performances are good as well in dynamics as in statics). By comparing the simulation results, it can be seen that all controllers offer good speed tracking performances. However, the fixed structure controller (second-order transfer function) is a more appropriate form for real implementation where the control system structure and complexity are constrained.

In order to assess the performance of the proposed controllers over a wide operating range of the motor, a desired speed profile including the acceleration and the speed are variable over time. The speed controller tracking performance is shown in Figure 12(a), the corresponding current profile is shown in Figure 12(b),

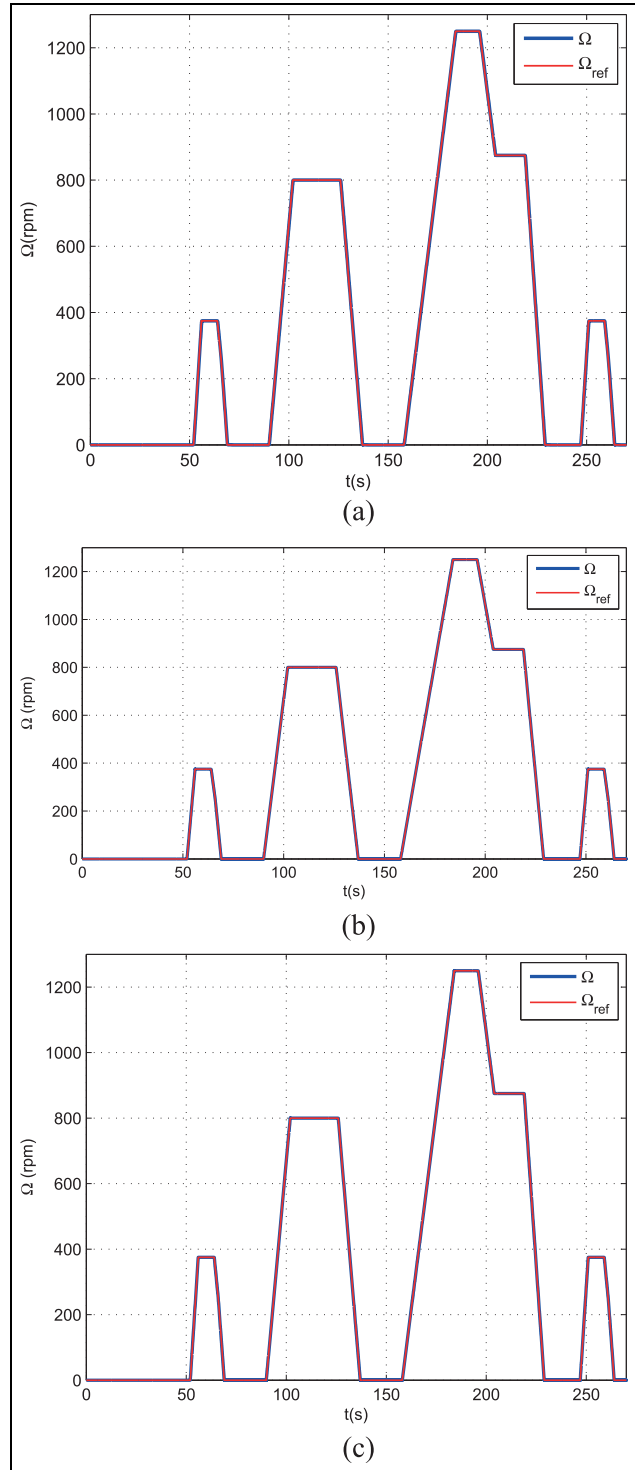


Figure 11. SRM speed response for the ECE-15 cycle: (a) classical PI controller, (b) full-order H_∞ controller, and (c) fixed structure H_∞ controller.

while Figure 12(c) illustrates the torque motor response against the load torque. This load torque is considered as an external disturbance with an amplitude of 1 Nm applied on the interval [1.5 s, 2.5 s] and a step of

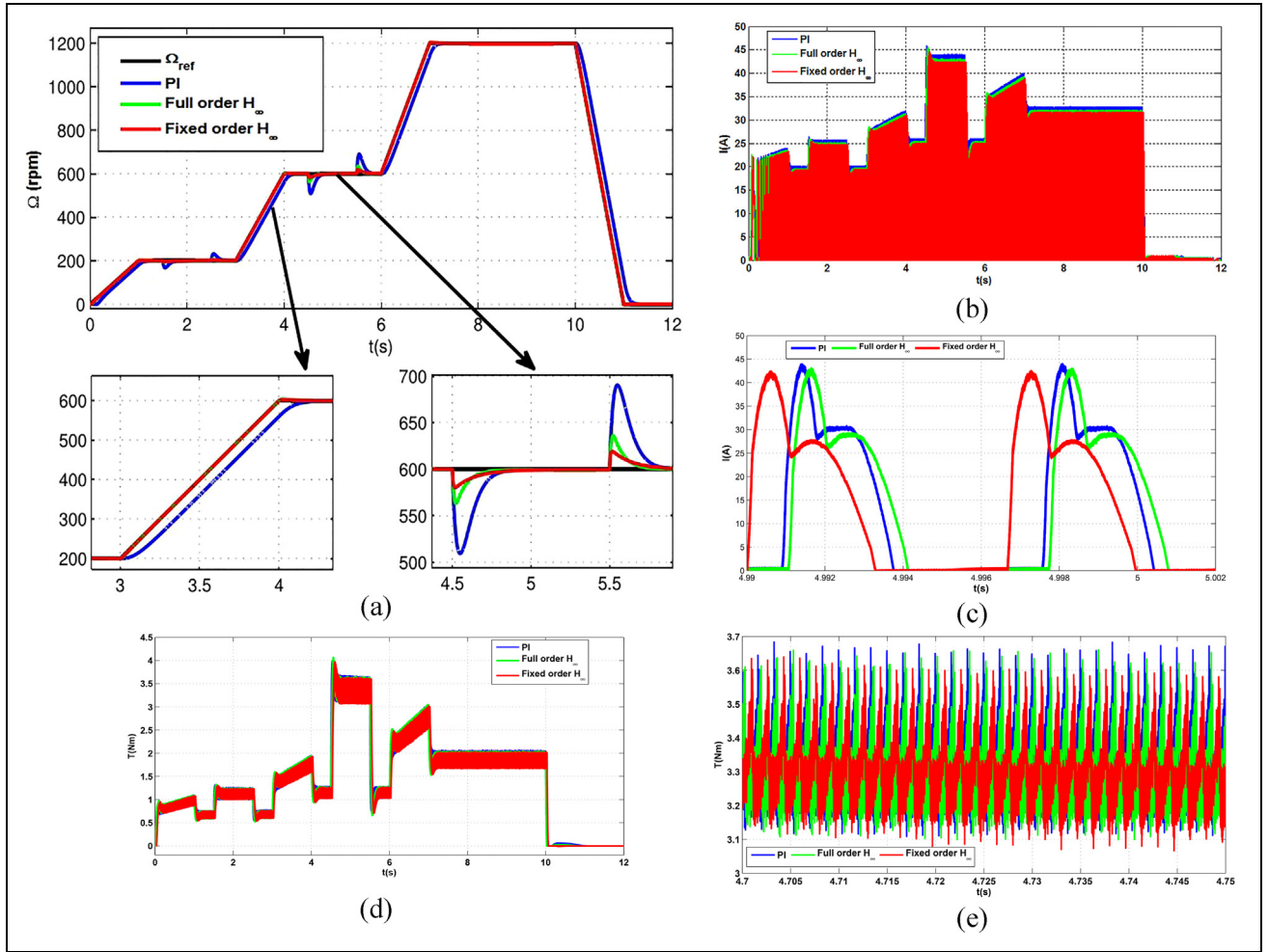


Figure 12. Comparative simulation results of PI, full-order H_∞ , and fixed structure H_∞ controllers: (a) SRM speed profile, (b) current response, (c) zoom into current response, (d) torque response, and (e) zoom into torque response.

amplitude of 3.2Nm applied on the interval [4.5s; 5.5s]. From Figure 12(a), we can see that the robust controllers track the desired speed without steady-state error for ramp. Both H_∞ speed controllers are steered to the desired one, and the tracking and disturbance rejection is achieved faster than the proportional–integral (PI) controller. Figure 12(c) is obtained by zooming into Figure 12(b). It illustrates the current regulation of one motor phase for all the designed current controllers. It can be observed that all the controllers ensure a good performance tracking. It can be also seen in Figure 12(d) that the torque ripple is small. It is around 15% and 13.4% of the requested motor torque for both full- and fixed-order H_∞ controllers, respectively, as depicted in Figure 12(e).

Current control. Simulations are carried out for the two synthesized H_∞ current controllers. The turn-on and turn-off angles of the SRM switching policy are chosen to be 0° and 180° , respectively. We carried out this

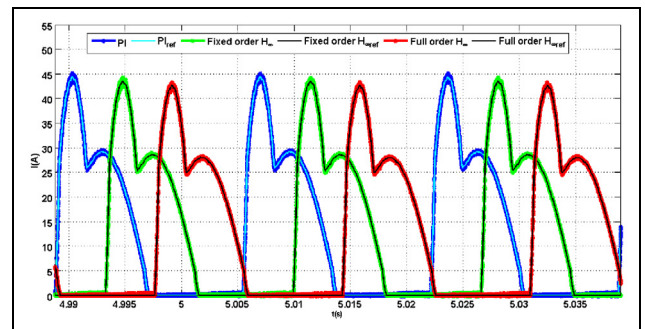


Figure 13. Comparative simulation results of current responses at a constant speed of 1000 r/min.

simulation test to compare the three current controllers where SRM phase’s current forms are shown in Figure 13 for a constant speed (1000r/min), on one hand, and on the other hand, another test is performed to compare the current step responses (see Figure 14).

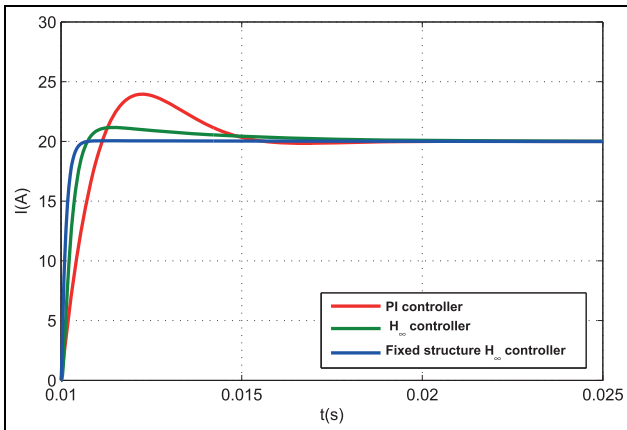


Figure 14. Current step response comparison.

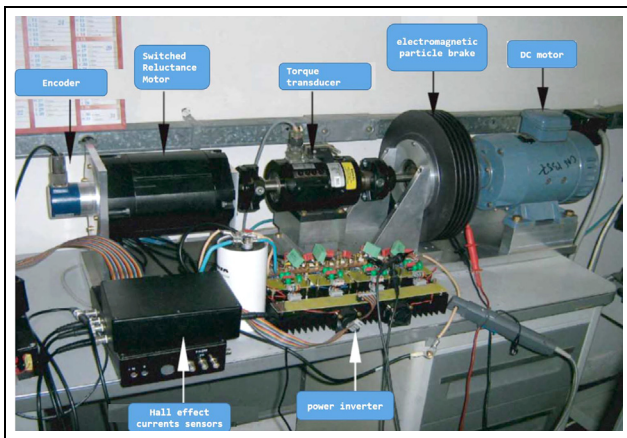


Figure 15. Experimental test bench of GeePs Laboratory.

From these simulation results of the proposed current controllers, it can be seen that all controllers offer good current tracking with high performances. As seen before, the fixed structure controller seems to be a better choice for a practical implementation since it provides a good control performance as well as a relatively good robustness and a reduced complexity of the controller structure.

Experimental results

Experimental tests are carried out on the test bench shown in Figure 15. A block diagram of this test bench is given in Figure 16. It is based on an SRM coupled to an electromagnetic particle brake used as load torque unit, a power inverter (asymmetric half bridge converter), and a dSPACE 1005 control unit with a sampling time of $100\ \mu\text{s}$. Furthermore, the test bench is also equipped with a torque transducer to measure the mean torque (Honeywell model: 1104-500, capacity: $55\ \text{N m}$), an encoder to measure the angular position and speed of the motor, and four Hall effect sensor to measure the electric phase currents.

Besides the simulation results, experimental results are performed to validate the proposed simulation approaches. Experimental measurements of speed, currents, and torque are presented in Figure 17. The SRM speed increases in order to reach the speed of $200\ \text{r/min}$, and the SRM runs at this speed for $3\ \text{s}$ and then accelerates to track the desired speed of $600\ \text{r/min}$, and evolved with this speed for $3\ \text{s}$, thereafter at $t = 7\ \text{s}$, the SRM accelerates once again to track the desired velocity of $1000\ \text{r/min}$. At $t = 10\ \text{s}$, the SRM carries out a

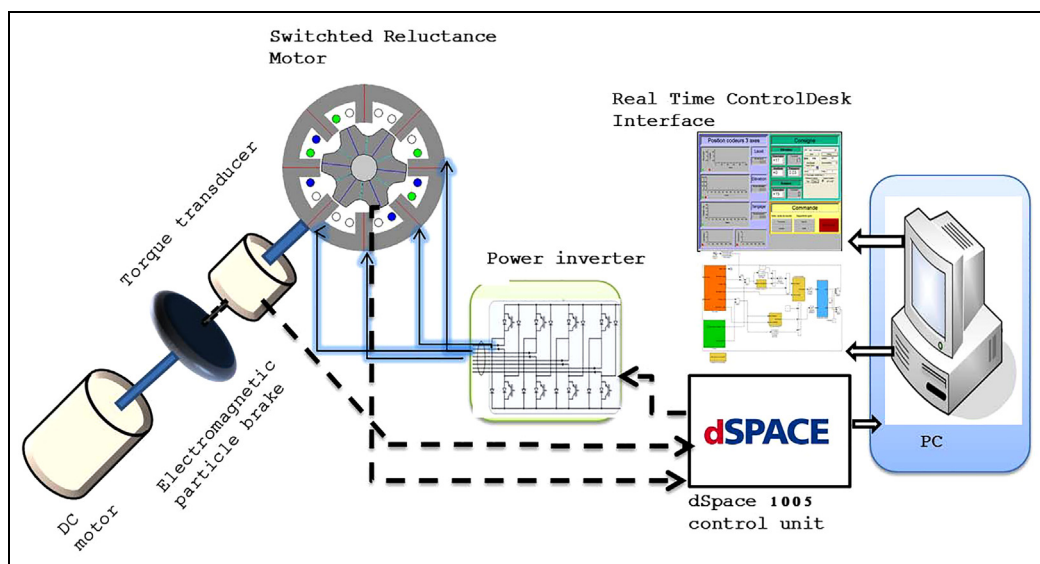


Figure 16. Block diagram of the test bench.

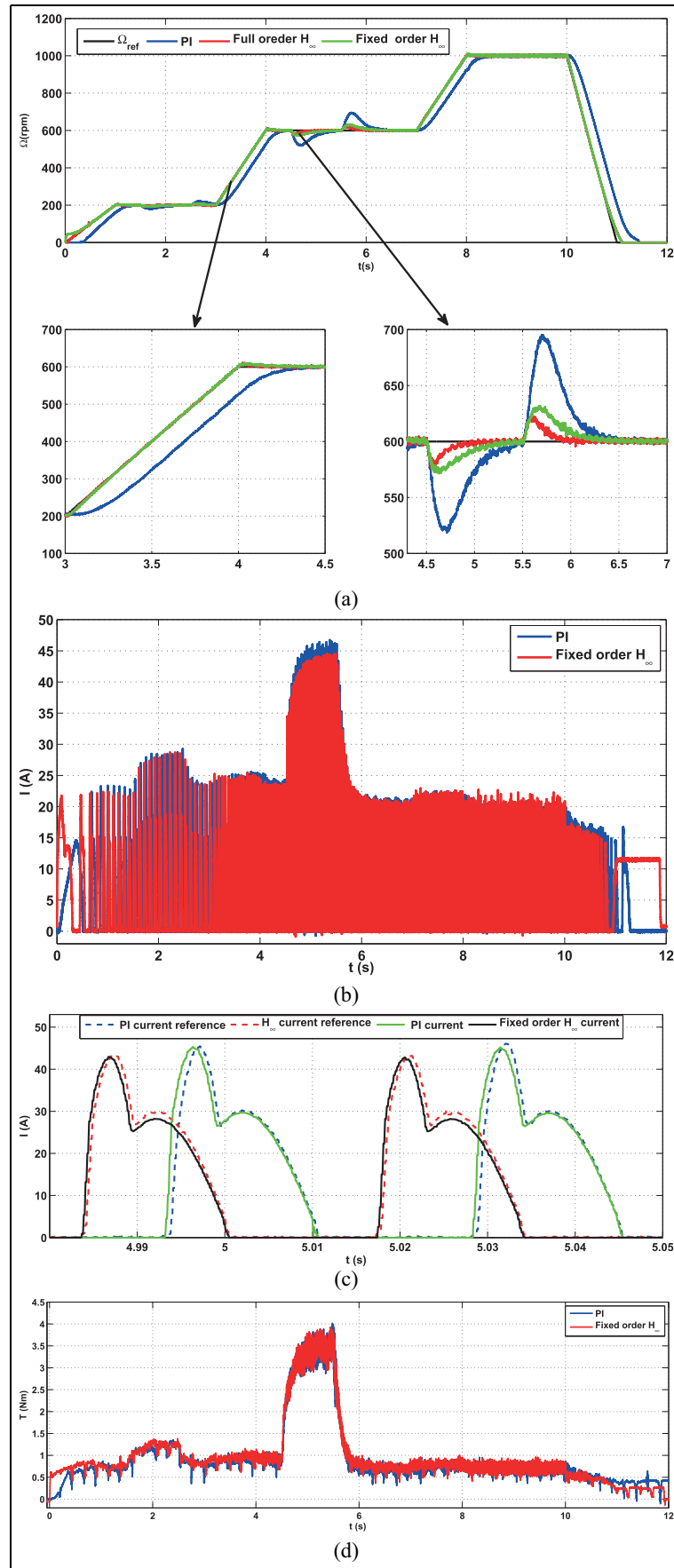


Figure 17. Comparative experimental results of PI, full-order H_∞ , and fixed structure H_∞ controllers. (a) SRM speed profile, (b) current response, (c) zoom current response, and (d) torque response.

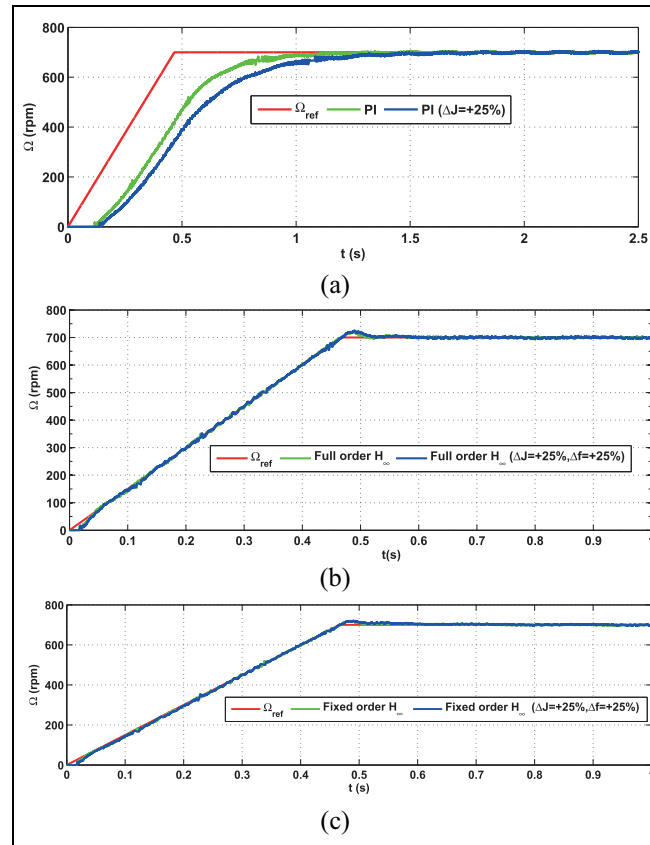


Figure 18. Robustness tests of the speed controllers with respect to the mechanical parameter uncertainties (J , f). (a) PI, (b) full-order H_{∞} , and (c) fixed structure H_{∞} .

deceleration until to stop. The speed profile is given in Figure 17(a), and we note that this scenario is carried out with success. It can be seen that the control requirements are achieved. These results are relatively close to the simulations one.

Robustness tests. In order to examine the robustness of the proposed controllers, further tests were performed by introducing mechanical and electrical parameter variations. For this purpose, the motor mechanical and electrical parameter values used for the robust control design are increased by 25% compared to their nominal values. The tests were conducted for the mechanical and electrical parameter variations separately. The resistance, inductance for the inner loop, moment of inertia, and friction coefficient for the outer one were increased by 25% compared to their nominal values, and the experiment results are depicted in Figures 18 and 19. These figures illustrate the speed responses of SRM and currents phase responses under these parameter variations. From these figures, we can see that the control system still turned out to be stable. Furthermore, the proposed controllers present a good reference tracking and ensure the robustness with respect to these parametric variations.

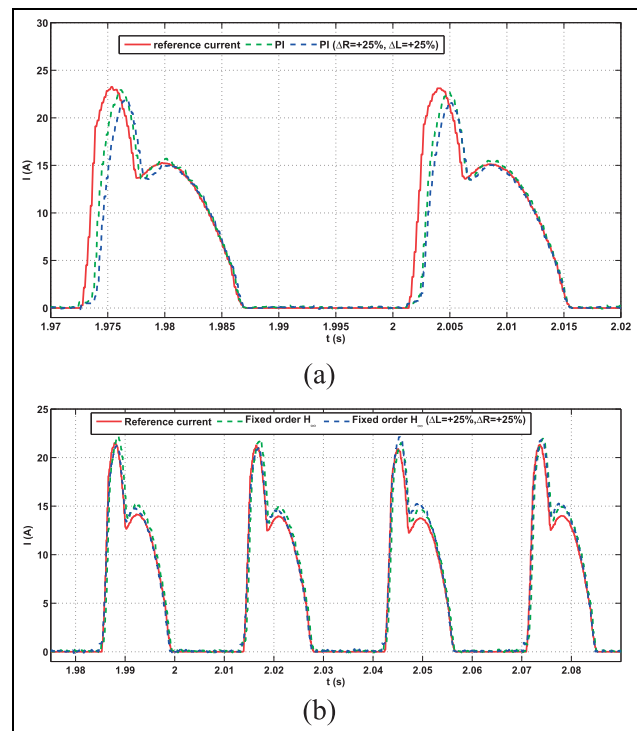


Figure 19. Robustness tests of the current controllers with respect to the electrical parameter uncertainties (L , R). (a) PI, (b) full-order H_{∞} , and (c) fixed structure H_{∞} .

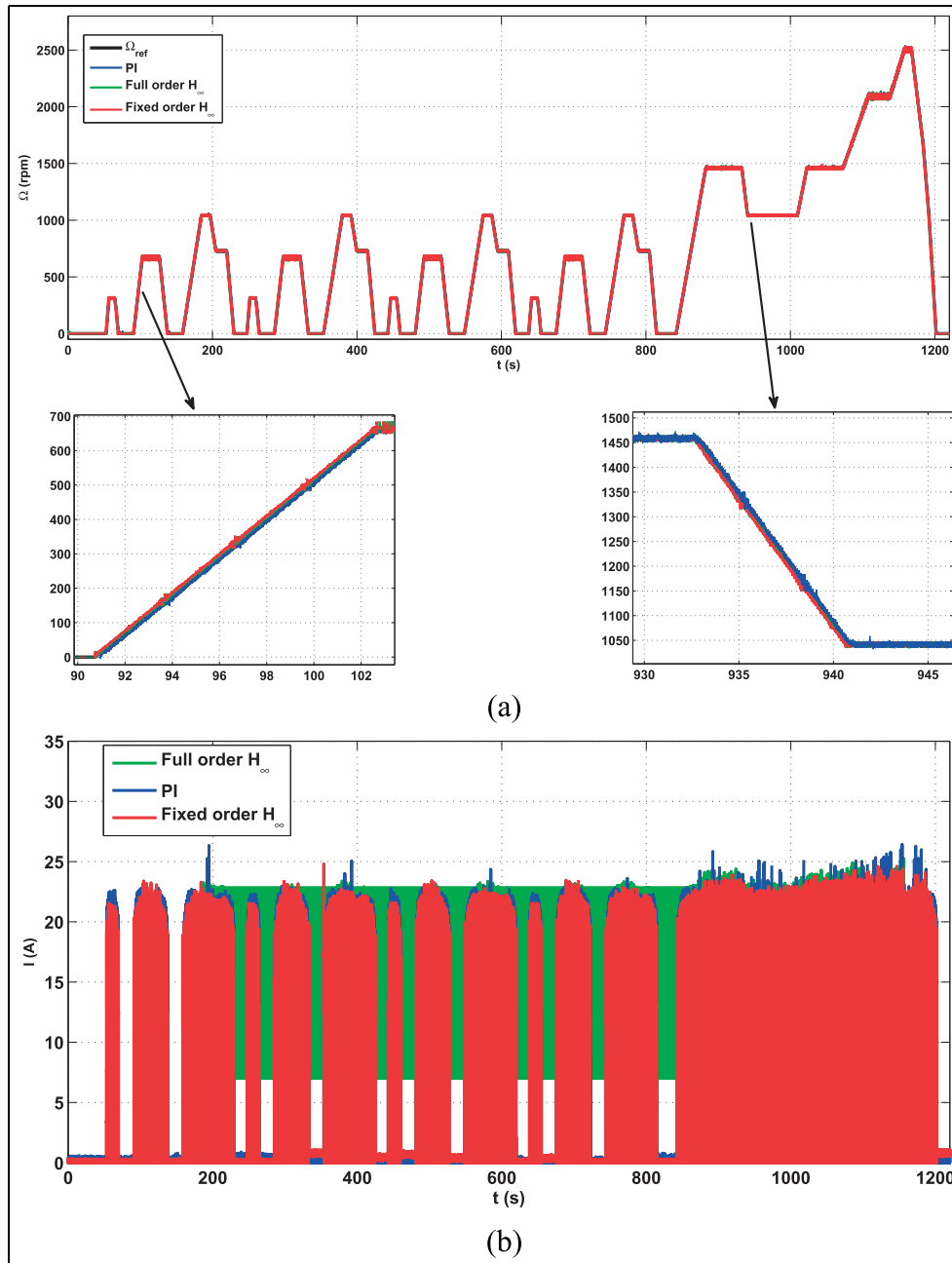


Figure 20. Experimental NEDC cycle: (a) speed profile driving cycle and (b) current response.

In the interest of EV application, the proposed controller approaches are evaluated with new European driving cycle (NEDC), which represents the typical usage of vehicle in Europe. It consists of four repeated ECE-15 urban driving cycles (UDCs) and one extra urban driving cycle (EUDC). The test includes a scenario of driving speed pattern with accelerations, constant speed cruises, and decelerations. This cycle thus constitutes an interesting study support to evaluate the performances of the proposed control approaches in various operating ranges of vehicle. The obtained

results from this test are shown in Figure 20 and confirm that the proposed fixed H_∞ control approach is very interesting for EV application.

Conclusion

In this article, a new SRM drive design control is proposed for electrical vehicle applications. It consists in a cascaded architecture that regulates the speed (outer loop) and the current (inner loop). In the proposed cascade control structure, two different (standard and

fixed H_∞) approaches are adopted for speed and current loops. Robustness analysis and simulation results confirm that all designed controllers guarantee a robustness margin with good dynamic and static performances. The fixed H_∞ controller gives a comparable robustness performance to full-order controller. However, the fixed structure controller presents the best choice for a practical implementation in an EV because the order of the H_∞ standard is very high. This makes them ideally suited for real-world applications where the control system structure and complexity are constrained. Thereafter, appreciable performances and robustness of SRM are assessed by simulation. Finally, an experimental evaluation of the proposed control scheme is highlighted. The main purposes were to maintain both performance and robustness of SRM under external disturbances and parameter variations.

Declaration of conflicting interests

The author(s) declared no potential conflicts of interest with respect to the research, authorship, and/or publication of this article.

Funding

The author(s) received no financial support for the research, authorship, and/or publication of this article.

References

1. Raisemche A, Boukhniher M and Diallo D. New fault tolerant control architectures based on voting algorithms for electric vehicle induction motor drive. *T I Meas Control* 2015; 38: 1120–1135.
2. Boukhniher M and Raisemche A. *Fault tolerant control for induction motor in electrical vehicle*. In: *2012 IEEE international conference on control applications (CCA)*, Dubrovnik, 3–5 October 2012, pp.136–141. New York: IEEE.
3. Yaling W, Yanliang X, Yufang W, et al. Outer rotor switched reluctance motor and its control system used in electric vehicles. In: *International conference on electrical machines and systems*, Beijing, China, 20–23 August 2011, pp.1–4. New York: IEEE.
4. Xue XD, Cheng KWE and Cheung NC. Selection of electric motor drives for electric vehicles. In: *Power engineering conference*, Padova, 1–4 September 2008, pp.1–6. New York: IEEE.
5. Alrifait TM, Zribit M and Ramirez HS. Static and dynamic sliding mode control of variable reluctance motors. *Int J Control* 2004; 77: 1171–1188.
6. Dong Hee K, Hae Gwang J and Kyo Beum L. Torque ripple minimization of switched reluctance motors based on fuzzy logic and sliding mode control. In: *IEEE international symposium on industrial electronics*, Taipei, Taiwan, 28–31 May 2013, pp.1–6. New York: IEEE.
7. Jie X and Changliang X. Fuzzy logic based adaptive PID control of switched reluctance motor drive. In: *Chinese control conference*, Hunan, China, 26–31 July 2007. New York: IEEE.
8. Rahman KM, Gopalakrishnan S, Fahimi B, et al. Optimized torque control of switched reluctance motor at all operational regimes using neural network. *IEEE T Ind Appl* 2001; 37: 904–913.
9. Doyle J, Glover K, Khargonekar PP, et al. State space solutions to standard H_2 and H_∞ control problems. *IEEE T Autom Contr* 1989; 34: 831–847.
10. Stein G and Doyle JC. Beyond singular values and loop shapes. *J Guid Control Dynam* 1991; 14: 5–16.
11. Gouatarbes J, Boukhniher M, Ferreira A, et al. Robust control for ultrasonic motor operating within harsh environments. In: *2007 IEEE/ASME international conference on advanced intelligent mechatronics*, Zurich, 4–7 September 2007, pp.1–6. New York: IEEE.
12. Boukhniher M, Chaibet A and Larouci C. Experimental H-infinity robust control of aerial vehicle flight. In: *2011 19th Mediterranean conference on control & automation (MED)*, Corfu, 20–23 June 2011, pp.242–247. New York: IEEE.
13. Ouddah N, Boukhniher M, Chaibet A, et al. Robust controller designs of switched reluctance motor for electrical vehicle. In: *2014 22nd Mediterranean conference of control and automation (MED)*, Palermo, 16–19 June 2014, pp.212–217. New York: IEEE.
14. Rodrigues M, Costa Branco PJ and Suemitsu W. Fuzzy logic torque ripple reduction by turn off angle compensation for switched reluctance motors. *IEEE T Ind Electron* 2001; 48: 711–715.
15. Cudrut V and Gabriel A. Nonlinear and identification of a switched reluctance motor. In: *IFAC symposium on nonlinear control systems*, Stuttgart, 1–3 September 2004. Elsevier.
16. Sahoo NC, Xu JX and Pandau SK. Low torque ripple control of switched reluctance motors using iterative learning. *IEEE T Energ Conver* 2001; 16: 318–326.
17. Tingna S, Longtao N and Wenshan L. Torque ripple minimization in switched reluctance motors using sliding mode variable structure control. In: *Proceedings of the 29th Chinese control conference*, Beijing, China, 29–31 July 2010. New York: IEEE.
18. Apkarian P and Noll D. Non smooth h_∞ synthesis. *IEEE T Automat Contr* 2006; 51: 71–86.
19. Zhou K and Doyle JC. *Essentials of robust control*. Upper Saddle River, NJ: Prentice Hall, 1998.